

1 **Secondary Organic Aerosols Derived from Intermediate Volatility**
2 **n-Alkanes Adopt Low Viscous Phase State**

3 Tommaso Galeazzo¹, Bernard Aumont², Marie Camredon², Richard Valorso², Yong B. Lim³,
4 Paul J. Ziemann^{4,5}, and Manabu Shiraiwa^{1,*}

5

6

7 1. Department of Chemistry, University of California, Irvine, CA92625, USA

8 2. Univ Paris Est Creteil and Université Paris Cité, CNRS, LISA, F-94010 Créteil, France

9 3. California Air Resources Board, Riverside, CA92507, USA

10 4. Department of Chemistry, University of Colorado, Boulder, Colorado, USA

11 5. Cooperative Institute for Research in Environmental Sciences (CIRES), University of
12 Colorado, Boulder, Colorado, USA

13

14

15 * Correspondence to: m.shiraiwa@uci.edu

16

17 **Abstract.**

18 Secondary organic aerosol (SOA) derived from n-alkanes, as emitted from vehicles and volatile
19 chemical products, is a major component of anthropogenic particulate matter, yet **the** chemical
20 composition and phase state are poorly understood and **thus poorly** constrained in aerosol
21 models. Here we provide a comprehensive analysis of n-alkane SOA by explicit gas-phase
22 chemistry modeling, machine learning, and laboratory experiments to show that n-alkane SOA
23 adopt low viscous semisolid or liquid states. Our study underlines the complex interplay of
24 molecular composition and SOA viscosity: n-alkane SOA with higher carbon number mostly
25 consists of less functionalized first-generation products with lower viscosity, while the lower
26 carbon number SOA contains more functionalized multigeneration products with higher
27 viscosity. This study opens up a new avenue for analysis of SOA processes and the results
28 indicate little kinetic limitations of mass accommodation in SOA formation, supporting the
29 application of equilibrium partitioning for simulating n-alkane SOA formation in large-scale
30 atmospheric models.

31

32 **Introduction**

33 Secondary organic aerosol (SOA) **is** ubiquitous in the atmosphere, affecting climate, air
34 quality and public health (Pöschl and Shiraiwa, 2015; Jimenez et al., 2009). They are generally
35 formed by multigenerational oxidation of volatile organic compounds (VOCs) emitted by both
36 anthropogenic and biogenic sources followed by condensation of semi-volatile oxidation
37 products into the particle phase (Ziemann and Atkinson, 2012; Kroll and Seinfeld, 2008). As
38 an important class of SOA precursors, there is a growing attention to intermediate volatile
39 organic compounds (IVOCs), which can partition to the gas phase upon dilution of primary
40 organic aerosols after fresh emission sources such as vehicle tailpipes, combustion of fossil and
41 fuel oils, and volatile chemical products (Robinson et al., 2007; McDonald et al., 2018). The
42 inclusion of IVOCs in the model simulations helps to reduce the gap between model simulation
43 and field observation of SOA (de Gouw et al., 2011; Li et al., 2022; Zhao et al., 2016).

44 SOA can adopt different particle phase states (liquid, amorphous semisolid, and glassy
45 solid), depending on their chemical composition, relative humidity and temperature (Virtanen
46 et al., 2010; Petters et al., 2019; Reid et al., 2018; Renbaum-Wolff et al., 2013) and also
47 evolving upon chemical aging and photochemistry (Baboomian et al., 2022). SOA phase state
48 plays an important role in a number of atmospheric multiphase processes (Shiraiwa et al., 2017).
49 The occurrence of glassy SOA in the free troposphere can impact activation pathways of ice
50 crystals and cloud droplets (Knopf and Alpert, 2023). Slow diffusion in viscous particles

51 induces kinetic limitations in heterogeneous and multiphase reactions (Zhang et al., 2018; Zhou
52 et al., 2019; Shiraiwa et al., 2011), affecting long-range transport (Shrivastava et al., 2017; Mu
53 et al., 2018). The timescale of SOA partitioning can be prolonged in viscous particles
54 (Schervish and Shiraiwa, 2023), retarding uptake of semi-volatile compounds and mixing of
55 different particle populations (Ye et al., 2016). Particle phase state also modulates SOA growth
56 to cloud condensation nuclei sizes, affecting cloud life cycle (Zaveri et al., 2022). While the
57 phase states of SOA generated by biogenic VOCs such as terpenes and isoprene have been
58 extensively studied (Virtanen et al., 2010; Petters et al., 2019; Renbaum-Wolff et al., 2013;
59 Baboomian et al., 2022; Zhang et al., 2018), those derived from IVOCs are hardly investigated
60 and remain poorly constrained.

61 Viscosity (η) is a dynamic property that characterizes the particle phase state, which can
62 be derived from the glass transition temperature (T_g) of the constituting species (Koop et al.,
63 2011). Several structure-activity relationships models have been developed to predict the T_g of
64 an organic compound using various molecular properties including molar mass, atomic O:C
65 ratio (Shiraiwa et al., 2017), elemental composition (DeRieux et al., 2018), and volatility (Li et
66 al., 2020; Zhang et al., 2019). A method was developed to predict SOA viscosity from the T_g -
67 scaled Arrhenius plot of fragility by considering Gordon-Taylor mixing rule and hygroscopic
68 growth of SOA particles (DeRieux et al., 2018; Shiraiwa et al., 2017). The T_g compositional
69 parameterizations (CP) and the viscosity prediction method have been applied to high
70 resolution mass spectrometry data of various types of SOA including toluene SOA (DeRieux
71 et al., 2018), SOA generated by diesel fuels (Song et al., 2019), β -caryophyllene SOA (Maclean
72 et al., 2021), and SOA generated by surrogate VOC mixtures by healthy and stressed plants
73 (Smith et al., 2021), agreeing well with viscosity measurements. However, CP substantially
74 overestimated viscosity measurements of indoor surface films which are mostly composed of
75 unsaturated high molar mass compounds such as triglycerides (O'Brien et al., 2021). CP does
76 not consider molecular structure nor functionality explicitly, representing a limitation of this
77 method. Galeazzo and Shiraiwa (2022) overcame this limitation by developing a machine
78 learning-based model, tgBoost, with an application of cheminformatics “molecular
79 embeddings” that retains detailed information on atomic composition, molecular structure and
80 connectivity. The main novel feature introduced by tgBoost is model capability to predict
81 different T_g for structural isomers and high sensitivity of T_g to various functional groups,
82 consistent with viscosity measurements for functionalized compounds (Rothfuss and Petters,
83 2017; Grayson et al., 2017).

84 Long-chain linear alkanes (n-alkanes) are representative IVOCs and account for a
85 substantial fraction of non-methane hydrocarbons in urban air as mainly emitted from
86 anthropogenic activities such as vehicle exhausts and incomplete fuel combustion (Li et al.,
87 2022). Gas-phase oxidation of n-alkanes by OH radicals can trigger the formation of SOA with
88 high yields, as observed in laboratory experiments (Aimanant and Ziemann, 2013a; Lim and
89 Ziemann, 2009b; Srivastava et al., 2022) and field observations (Gentner et al., 2012; Li et al.,
90 2022). Gas-phase oxidation pathways of n-alkanes are relatively well understood and
91 successfully simulated by detailed gas-phase chemistry modeling (Aumont et al., 2012; La et
92 al., 2016), but the chemical composition of n-alkane SOA has only been characterized well for
93 the C₁₆ n-alkane (Ranney et al., 2023) and the phase state and viscosity of alkane SOA are
94 unknown. Therefore, the n-alkane SOA system provides an ideal benchmark for the
95 investigation of the interplay of chemical composition, particle phase state and kinetic
96 limitations influencing SOA growth and evolution.

97 In this study, we implemented tgBoost in an explicit gas-phase chemistry model
98 GECKO-A to investigate the complex interplay of chemical composition, kinetic partitioning,
99 and phase state of n-alkane SOA generated under dry and high NO_x conditions. The GECKO-
100 A model is one of the most comprehensive generators of gas-phase chemical schemes to date,
101 as it automatically generates detailed gas-phase chemical mechanisms involving thousands to
102 millions of oxidation products from a given VOC precursor based on established reaction
103 pathways and structure–activity relationships (Aumont et al., 2012; La et al., 2016). The
104 simulations were conducted with variable effective mass accommodation coefficient to
105 consider potential kinetic limitations in amorphous semisolid particles (Shiraiwa and Pöschl,
106 2021). The simulated results were compared with chamber experimental data on SOA yields
107 (Lim and Ziemann, 2009b) as well as new measurements on thermal desorption temperatures
108 and functional group distributions.

109

110 **Methods:**

111 **Model simulations.**

112 We applied the Generator for Explicit Chemistry and Kinetics of the Organics in the
113 Atmosphere (GECKO-A) (Aumont et al., 2012; La et al., 2016) to obtain detailed reaction
114 schemes of gas-phase OH oxidation of n-alkanes along with rate constants. The GECKO-A
115 generator used for the oxidation of linear n-alkanes treats chemistry of peroxy (RO₂) and alkoxy
116 (RO) radicals. Under high NO_x conditions, RO₂ radicals mainly react with NO and NO₂, to
117 form closed-shell compounds or RO radicals, which undergo reaction with O₂, unimolecular

118 decomposition (i.e. C-C bond breaking) or isomerization, generating stable compounds and/or
119 to new RO₂ radicals. The detailed protocol for such mechanism generation is available in
120 previous studies (Aumont et al., 2013; Aumont et al., 2005; Aumont et al., 2012; La et al.,
121 2016). In this study, the generated chemical schemes include the description of the formation
122 of organic species up to four generations. Species with vapor pressure below 10⁻¹³ atm are
123 assumed to be of low enough volatility to completely partition to the condensed phase and their
124 gas phase chemistry is then not generated in the mechanism to reduce the mechanism (La et al.,
125 2016). The number of species treated in the model was ~10⁴ species for dodecane (C₈H₁₈) that
126 increases to ~10⁵ species for heptadecane (C₁₇H₃₆).

127 The latest structure-activity relationships are treated for the chemistry of organic
128 compounds with OH radical (Jenkin et al., 2018b, a; Jenkin et al., 2019), the bimolecular
129 reactions of peroxy radicals (Jenkin et al., 2019), as well as alkoxy radical decomposition and
130 H migration reaction rates (Vereecken and Peeters, 2009; La et al., 2016). The vapor pressures
131 of semi-volatile species were estimated by using Nannoolal's group contribution method
132 (Nannoolal et al., 2008) implemented in GECKO-A, as described in detail in Valorso et al.
133 (2011). The model treats unimolecular particle-phase reactions including cyclization of
134 hydroxyketones and dehydration of cyclic hemiacetals to form dihydrofurans (La et al., 2016).
135 The model does not treat autoxidation and dimerization in the gas phase, but these processes
136 should be minor pathways during n-alkane oxidation in the presence of high NO_x as the reaction
137 of peroxy radicals with NO_x should be dominant (Praske et al., 2018; Pye et al., 2019); thus,
138 their absence from GECKO-A chemical schemes should not have major impacts on the
139 simulated results.

140 These explicit chemical mechanisms were implemented into a box model to simulate
141 the multigenerational oxidation of n-alkanes, partitioning of oxidation products into the particle
142 phase based on their vapor pressures, and vapor wall loss to mimic chamber experiments (La
143 et al., 2016). We replicated the experimental conditions used in Lim and Ziemann (2009b) to
144 generate SOA from OH oxidation of C₈-C₁₇ n-alkanes at high NO_x conditions in the presence
145 of non-volatile dioctyl sebacate (DOS) seed particles with particle radius of 150 nm and mass
146 loading of 200 μg m⁻³. Temperature was held constant at 295.15 K, pressure was set at 1 atm
147 and RH was fixed at 0.5%. Photolysis frequencies were calculated based on the cross sections,
148 quantum yields as described in Aumont et al. (2005) and the photonic flux of blacklight lamps.
149 Each simulation ran for 1 hour and the time evolution of species concentration were computed
150 through a two-step method that solves stiff ordinary differential equations (Verwer, 1994;
151 Verwer et al., 1996). To investigate effects of mass concentrations, we also simulated

152 experiments of n-alkane photooxidation under high NO_x conditions with low mass loadings by
153 Presto et al. (2010). The number concentration of seed particles with particle diameter of 200
154 nm was ~5000 cm⁻³, corresponding to the mass concentration of ~20 μg m⁻³. Initial mixing
155 ratios of n-alkane and NO_x were in the range of 3 – 99 ppb and 1 – 5 ppm, respectively, as
156 reported in Presto et al. (2010) and these conditions were applied in the model.

157 The box model accounts for mass transfer kinetics of organic species between gas and
158 particle phases. Partitioning follows Raoult's law at equilibrium and partitioning kinetics are
159 described by the gas-particle mass transfer coefficient with the Fuchs-Sutugin approach
160 (Seinfeld and Pandis, 2016). For the base case scenario, we fixed the mass accommodation
161 coefficient (α) to be 1 based on molecular dynamics simulations (Julin et al., 2014), assuming
162 particles being low viscous liquids without kinetic limitations of bulk diffusion. To account for
163 potential kinetic limitations in viscous particles, we applied an effective mass accommodation
164 coefficient (α_{eff}) that is a function of volatility and bulk diffusivity (Shiraiwa and Pöschl, 2021):

$$165 \quad \alpha_{\text{eff}} = \alpha_s \frac{1}{1 + \frac{\alpha_s \omega C^0 r_p}{4 D_b \rho_p} \frac{10^{-12} \text{ g cm}^{-3}}{\mu\text{g m}^{-3}}} \quad (1)$$

166 where α_s is the surface accommodation coefficient assumed to be 1, ω (cm s⁻¹) is the mean
167 thermal velocity of the organic compound in the gas phase, r_p (cm) is the particle radius, ρ_p (g
168 cm⁻³) is the particle density, and C^0 (μg m⁻³) is the pure compound saturation mass
169 concentration. D_b (cm² s⁻¹) is bulk diffusivity as simulated by conversion of viscosity as detailed
170 below. α_{eff} values are shown as a function of D_b and vapor pressure p^0 in Fig A3a. We
171 accounted for a reversible gas-to-chamber wall partitioning of gases and assumed a fixed first-
172 order deposition rate constant of 5×10^{-4} s⁻¹ based on experimental observations and previous
173 modeling studies (Krechmer et al., 2016; La et al., 2016; Lim and Ziemann, 2009b). A
174 desorption rate constant from wall to the gas phase was derived by using a parameter of
175 $C_w/M_w \gamma_w$ of 9 μmole m⁻³ for n-alkanes and 120 μmole m⁻³ for oxidation products based on
176 chamber observations (Matsunaga and Ziemann, 2010), as discussed in La et al. (2016).
177 Potential concentration gradients in the particle phase are not resolved explicitly and SOA
178 particles are assumed to be homogeneously well-mixed.

179 The glass transition temperatures (T_g) of organic compounds were predicted by the
180 machine learning-based model tgBoost (Galeazzo and Shiraiwa, 2022) and the
181 parameterization based on elemental composition (DeRieux et al., 2018; Li et al., 2020). The
182 implementation of the compositional parametrization into the GECKO-A box model was done
183 in Galeazzo et al. (2021) with a thorough description of all the equations, assumptions and steps

184 adopted for the implementation of this viscosity estimation method. In this study, we
185 implemented tgBoost, a newly developed machine learning model for better predictions of T_g .
186 tgBoost is a powerful model that can discern compositional isomers by functionality and predict
187 the glass transition temperature of an organic compound i ($T_{g,i}$) with an uncertainty of ± 18.3 K
188 using the canonical SMILES notation of a molecule (Galeazzo and Shiraiwa, 2022). We have
189 implemented a pipeline (i.e., gecko2vec) into GECKO-A to predict T_g of compounds from the
190 chemical mechanism in a fast and computationally efficient manner. Gecko2vec executes three
191 main steps: first, it translates the IDs of the compounds of interest of the GECKO-A mechanism
192 into the respective canonical SMILES notations (translation step); second, it transforms the
193 canonical SMILES notations into the respective molecular embeddings (i.e., unique 300-
194 dimensional numerical representations of molecules; embedding step); and finally, the
195 pretrained tgBoost model and its weights are loaded and used to predict T_g of each species
196 (prediction step). Within the box model, the T_g of total SOA particles ($T_{g,org}$) resulting from the
197 combination of its organic component and water mixture is computed using the Gordon–Taylor
198 equation (Dette et al., 2014; Koop et al., 2011; Zobrist et al., 2008). $T_{g,org}$ can be converted to
199 viscosity based on the Vogel-Tammann-Fulcher approach assuming the fragility parameter of
200 10 (DeRieux et al., 2018). Viscosity is further converted into bulk diffusivity using the
201 fractional Stokes-Einstein equation with a fractional parameter of 0.93 and an effective
202 molecular radius of 0.5 nm (Evoy et al., 2019). For both model simulations with CP and
203 tgBoost, the particle number concentration is assumed to remain constant (coagulation is not
204 treated), while the particle radius evolves following the partitioning of organic compounds.

205

206 **Laboratory experiments.**

207 SOA particles were generated from OH oxidation of C₈-C₁₇ n-alkanes in a 5.9 m³ Teflon
208 environmental chamber filled with clean air under high NO_x conditions in the presence of non-
209 volatile dioctyl sebacate (DOS) seed particles, as described in detail elsewhere (Lim and
210 Ziemann, 2009b). Briefly, 1 ppm of n-alkane, 10 ppm of methyl nitrite, and 10 ppm of NO were
211 added to the chamber from a glass bulb, and ~ 200 – 400 $\mu\text{g m}^{-3}$ of seed particles were added
212 from an evaporation-condensation apparatus. Relatively high mass concentrations of seed
213 particles were used so that semi-volatile compounds would condense to particles, minimizing
214 vapor deposition to chamber walls (Zhang et al., 2014; Matsunaga and Ziemann, 2010).
215 Blacklights covering two of the chamber walls were then turned on for 60 min to form OH
216 radicals by methyl nitrite photolysis (Atkinson et al., 1981). The amount of n-alkane reacted
217 was measured by collecting Tenax[®] samples before and after the experiment and analyzing by

218 gas chromatography with flame ionization detection (GC-FID). Aerosol volume concentrations
219 were measured using a scanning mobility particle sizer (Docherty et al., 2005) and converted
220 to an SOA mass formed using a density of 1.06 g cm^{-3} . SOA mass yields (mass of SOA
221 formed/mass of n-alkane reacted) were calculated from the measured SMPS mass (corrected
222 for particle wall loss using the $\sim 20\% \text{ h}^{-1}$ decay in mass after the lights were turned off) and the
223 GC-FID analyses. The final SOA mass concentrations were in the range of $\sim 300 - 6000 \text{ } \mu\text{g m}^{-3}$
224 3 depending on precursors (Lim and Ziemann, 2009b). The SOA yields measured in these
225 experiments were reported previously (Lim and Ziemann, 2009b), but in light of a recent
226 comparison of the accuracy of our SMPS measurements with filter sampling the values reported
227 here are higher by a factor of 1.24 (Bakker-Arkema and Ziemann, 2021).

228 A temperature-programmed thermal desorption (TPTD) method was also used to
229 measure thermal desorption temperatures of DOS that was present as seed particles in n-alkane
230 SOA. Particles were sampled directly from the chamber into a thermal desorption particle beam
231 mass spectrometer (Tobias et al., 2000), where they were formed into a beam inside an
232 aerodynamic lens, transported into a high vacuum chamber, and impacted on a copper rod
233 vaporizer that was coated with a non-stick polymer and cooled to -40°C . Note that compounds
234 with vapor pressure $< 10^{-5} \text{ Torr}$ are estimated to undergo negligible evaporation with the
235 residence time of $\sim 0.2 \text{ s}$ in the aerodynamic lens (Tobias et al., 2000). After sampling for 30
236 min, the vaporizer was warmed by room air to -5°C and then heated at 2°C min^{-1} to 200°C .
237 Compounds desorbed according to volatility and entered a quadrupole mass spectrometer,
238 where they were ionized by 70 eV electrons prior to mass analysis. In one recent n-hexadecane
239 experiment, the composition of nitrate, hydroxyl, carbonyl (ketone + aldehyde), carboxylic
240 acid, ester, and peroxide functional groups in SOA was measured using derivatization-
241 spectrophotometric methods, with the amount of $-\text{CH}_2-$ groups calculated by difference
242 (Ranney et al., 2023). We note that in that experiment the SOA yield measured by filter
243 sampling was nearly identical to the one we measured previously after applying the above
244 correction.

245

246 **Results and discussion**

247 **SOA yields and viscosity.**

248 Figure 1 shows comparisons of measurements and modeling for (a) SOA yields, (b)
249 functional group distributions, (c) N:C ratios, and (d) O:C ratios. Figure 1(a) shows the
250 measured yields of SOA generated from the oxidation of n-alkanes ($\text{C}_n\text{H}_{2n+2}$; $n = 8 - 17$) (Lim
251 and Ziemann, 2009b). The model base case (black line) with mass accommodation coefficient

252 of 1 for all species represents no kinetic limitations in the particle phase and the results are
253 similar to previous simulations performed by La et al. (2016). Vapor wall loss was considered
254 based on experimental observations and previous modeling studies (Krechmer et al., 2016; La
255 et al., 2016; Lim and Ziemann, 2009b), which is important to account for as no wall loss would
256 lead to a significant overestimation of SOA yields, as shown in the black dotted line and was
257 discussed in detail in La et al. (2016). Both experimental and simulated SOA yields increase
258 with an increase of n , reflecting the decrease in volatility of the precursor and its oxidation
259 products (Shiraiwa et al., 2014). The observed SOA yield trend is consistent with measurements
260 by a thermal desorption particle beam mass spectrometer, showing that n-alkane SOA are
261 composed of less oxidized products with lower volatility for precursors with higher n (Lim and
262 Ziemann, 2009b, a).

263 The overall good agreement suggests that multigenerational chemistry in the gas phase
264 and partitioning of semi- and low-volatile products, as explicitly treated by GECKO-A box
265 modeling, are the dominant pathway of n-alkane SOA formation under these conditions. It also
266 suggests that peroxy radicals (RO_2) mainly react with NO_x , minimizing autoxidation and gas-
267 phase dimerization by $\text{RO}_2 + \text{RO}_2$ reactions. Good model agreement also suggests that particle-
268 phase oligomerization chemistry is not a dominant process, while particle-phase unimolecular
269 reactions including cyclization of hydroxyketones and dehydration of cyclic hemiacetals
270 forming dihydrofurans are treated in the model as they are important for the further oxidation
271 due to the presence of a double bond in the dihydrofurans (Lim and Ziemann, 2009a; La et al.,
272 2016). Thus, the GECKO-A model seemingly treats all essential processes for simulations of
273 n-alkane SOA formation under high NO_x conditions. Note that a very recent study suggested
274 that cyclic hemiacetals form acetal dimers in the particle phase for SOA formed from the
275 reaction of n-hexadecane SOA and OH/NO_x (Ranney et al., 2023). In addition, particle-phase
276 chemistry was shown to be substantial in n-alkane SOA formation under low NO_x conditions
277 through peroxyhemiacetal and oligomer formation (Shiraiwa et al., 2013; Ziemann and
278 Atkinson, 2012). The impact of such particle-phase chemistry may warrant further
279 investigations including model development and experimental studies.

280 To explore the potential impacts of particle phase state on SOA formation and
281 partitioning, we implemented an effective mass accommodation coefficient (α_{eff}) which can
282 effectively consider kinetic limitations of bulk diffusion and also account for the effect of vapor
283 pressure on partitioning kinetics for species with various volatilities (Shiraiwa and Pöschl,
284 2021). Bulk diffusivity evolves upon SOA formation, which can be derived by viscosity and T_g
285 as predicted from the machine learning-based tgBoost model (dashed green line in Fig. 1a) and

286 the compositional parametrization (CP, dashed orange line in Fig. 1a). The simulated SOA
287 yields with tgBoost are very similar to the base case scenario with $\alpha = 1$, while the application
288 of the CP leads to smaller SOA yields for $n = 15-17$. These results indicate that α_{eff} is close to
289 1 with little kinetic limitations of bulk diffusion for most cases, except some limitations are
290 predicted by CP for large precursors. Deviations of tgBoost and CP stem from the difference in
291 phase state and viscosity predicted by the two methods.

292 Figure 2(a) shows the simulated viscosity and corresponding bulk diffusivity of n-
293 alkane SOA. **Notably**, the two models predict contrasting trends. The simulated glass transition
294 temperature ($T_{\text{g,org}}$) of SOA is presented in Fig. A1. The CP predicts a decrease in $T_{\text{g,org}}$ for C₈₋
295 ₁₂ with the lowest $T_{\text{g,org}}$ of ~ 250 K, which is likely due to a decrease of O:C ratio (Fig. 1d) as
296 lower O:C ratio can lead to a decrease of T_{g} (DeRieux et al., 2018; Shiraiwa et al., 2017),
297 followed by an increase of $T_{\text{g,org}}$ with n to reach ~ 270 K with C₁₇. These values correspond to
298 viscosity of $10^4 - 10^6$ Pa s, indicating that n-alkane SOA adopts viscous semisolid phase state.
299 The increase of viscosity for larger precursors is apparently reasonable, as their oxidation
300 products would have higher molar mass which would generally correspond to higher $T_{\text{g,org}}$
301 (Koop et al., 2011; Shiraiwa et al., 2017). Based on the Stokes-Einstein relation, bulk diffusivity
302 would be in the range of $3 \times 10^{-15} - 10^{-12}$ cm² s⁻¹. The characteristic timescale of bulk diffusion
303 in an average particle diameter of 300 nm can be as low as ~ 2 hours (Shiraiwa et al., 2011),
304 which is longer than experimental timescale of one hour. These low diffusivities and long
305 diffusion timescale can induce concentration gradients in the particle bulk, reducing α_{eff} to
306 cause significant kinetic limitations to retard SOA growth, which is not consistent with the
307 measured SOA yields.

308 tgBoost predicts the opposite trend, predicting a monotonic decrease of $T_{\text{g,org}}$ and
309 viscosity with an increase of n , suggesting that SOA phase state shifts from an amorphous
310 semisolid state ($10^2 < \eta < 10^5$ Pa s) towards a liquid-like phase state ($\eta < 10^2$ Pa s). These
311 results are counter-intuitive as T_{g} values of n-alkanes increase with an increase of n , which can
312 be reproduced with great precision by tgBoost (Galeazzo and Shiraiwa, 2022). The
313 determinants explaining this unexpected trend are chemical composition and molecular
314 structure of the oxidation products as discussed below. The characteristic timescale of bulk
315 diffusion is less than one second in a low viscous state and high bulk diffusivity (Shiraiwa et
316 al., 2011) and SOA particles are expected to be homogeneously well-mixed. Hence, α_{eff} remains
317 very close to 1 with little kinetic limitation of bulk diffusion.

318 Unfortunately, no direct viscosity measurements of n-alkane SOA generated under high
319 NO_x conditions are available to date, while there are two studies for n-alkane SOA generated
320 under NO_x-free conditions. Saukko et al. (2012) (Saukko et al., 2012) observed that n-
321 heptadecane (C₁₇H₃₆) SOA with low O:C ratio did not bounce from an impactor plate. It
322 indicates that these particles adopted a liquid-like state, as indicated by the violet shading in
323 Fig. 2(a), which is consistent with the tgBoost prediction. Shiraiwa et al. (2013) estimated bulk
324 diffusivity of n-dodecane (C₁₂H₂₆) SOA generated without NO_x to be 10⁻¹² cm² s⁻¹ using a
325 kinetic multilayer model to simulate evolution of particle size distribution. While these two data
326 points cannot be directly compared with the viscosity predictions of high NO_x n-alkane SOA,
327 they serve as reference data points for now and direct viscosity or bulk diffusivity
328 measurements of high NO_x n-alkane SOA are warranted in future studies.

329 Figure 2(b) shows the thermal desorption profiles of DOS that was present as seed
330 particles within the SOA formed from oxidation of the n-alkanes. Since DOS desorption
331 involved diffusion through the SOA prior to escape into vacuum, these profiles provided a
332 means for probing the SOA viscosity. The peaks in the DOS profiles for the C₈₋₁₃ and C₁₄₋₁₇ n-
333 alkanes are closely grouped, with vaporizer temperature at ~80 °C and ~65 °C, respectively,
334 with the peak for pure DOS occurring in between at ~72°C. The observed decrease in desorption
335 temperatures from low to high carbon numbers suggests an increase in effective volatility of
336 DOS in SOA generated from larger n-alkanes. In addition, Lim and Ziemann (2009) have
337 observed that C₁₀ n-alkane SOA generated under high NO_x conditions evaporate at higher
338 temperatures compared to C₁₂ and C₁₅ n-alkane SOA based on total ion thermal desorption
339 measurements (Lim and Ziemann, 2009b). Volatility and *T_g* were shown to exhibit clear
340 anticorrelation (Li et al., 2020); hence, these results strongly indicate that C₈₋₁₃ SOA have higher
341 *T_g* and viscosity compared to C₁₃₋₁₇ SOA. Note that the C₁₃ profile is bimodal with peaks at
342 ~80 °C and ~65 °C (Fig. 2b), which is in line with tgBoost prediction that the viscosity of C₁₃
343 alkane SOA is at the edge of amorphous semi-solid and liquid phase states (Fig. 2a). These
344 results indicate that n-alkane SOA generated by larger precursors adopt low viscous liquid-like
345 states, while n-alkane SOA generated by smaller precursors adopt viscous semisolid states, in
346 agreement with tgBoost predictions. The major strength of tgBoost is that it considers molecular
347 structure and functionality for *T_g* predictions, while the compositional parameterization does
348 not account for this effect, leading to intuitive but erroneous predictions.

349

350 **Chemical composition of SOA.**

351 Figure 1 also shows the simulated (c) N:C and (d) O:C ratios of SOA with $\alpha = 1$ (black
352 line) and $\alpha = \alpha_{\text{eff}}$ with T_g determined with tgBoost (green line) or the compositional
353 parameterization (orange line). The N:C ratio is very similar among all simulations being ~ 0.2
354 for C_8 and decreasing progressively to ~ 0.03 with each addition of a carbon atom in the
355 precursor. O:C ratios were calculated in two different ways by treating a nitrate ($-\text{ONO}_2$) group
356 to contain either three (solid lines) or one (dashed lines) oxygen atoms. One oxygen atom is
357 also considered because O:C ratios reported from aerosol mass spectrometer measurements
358 generally treat a nitrate group the same as a hydroxyl group, since they have the same effect on
359 oxidation state (Farmer et al., 2010). Similar to the N:C ratio, there is a constant decrease in
360 O:C of SOA with increasing n , which is consistent with previous measurements for n-
361 pentadecane ($C_{15}H_{32}$) SOA (Aimanant and Ziemann, 2013a) and n-hexadecane ($C_{16}H_{34}$) SOA
362 in this study, even though the simulated values are $\sim 45\%$ and 15% lower than the measured
363 N:C and O:C ratios, respectively. The discrepancies are likely due to errors on modeling gas-
364 wall partitioning and gas-particle partitioning. The difference may also be caused by missing
365 processes in the model such as reactive uptake of oxidants and particle-phase chemistry.

366 We measured functional group distributions in n-hexadecane SOA using derivatization-
367 spectrophotometric methods described in Aimanant and Ziemann (2013b), as shown in Fig.
368 1(b) and summarized in Table A1. Experimental measurements report high presence of $-\text{CH}_2-$
369 (13.81) and $-\text{ONO}_2$ (0.91), followed by ROH (0.41), $\text{RC}(=\text{O})$ (0.38), and $\text{RC}(=\text{O})\text{OR}$ (0.28),
370 with the average measured number of groups per C_{16} molecule in parenthesis. Figure 1(b)
371 includes simulation results by GECKO-A with CP and tgBoost, showing overall satisfactory
372 agreement. The simulated results with tgBoost show excellent agreement for hydroxyl and
373 methylene groups, while the simulated nitrates and carbonyls (ketones + aldehydes) are lower
374 than the measurements. The simulation by CP has also a similar trend, but with significantly
375 lower presence of nitrates, carbonyls, and esters.

376 Figure 3(a) shows the top 15 oxidation products in the particle phase formed by the
377 oxidation of n-hexadecane simulated by GECKO-A box model with tgBoost. Note that
378 positional isomers are lumped into one species and that the five species in the first row
379 constitute majority ($\sim 86\%$) of SOA mass. The simulated SOA is composed mostly by 1st
380 generation products including alkyl nitrates, hydroxynitrates, and hydroxyketones. There is also
381 a significant presence of 2nd and 3rd generation products such as esters and dinitrates. We also
382 **predicted** multi-functionalized decomposition products including smaller chain hydroxy
383 nitrates and alkyl lactones as well as particle-phase products from cyclization of
384 hydroxyketones and dehydration of cyclic hemiacetals to form dihydrofurans. A very recent

385 study by Ranney et al. (2023) measured n-hexadecane oxidation products under high NO_x,
386 finding that alkyl nitrates, hydroxyl nitrates, hydroxyl carbonyls, cyclic hemiacetals, and cyclic
387 hemiacetal nitrates were major products. These compounds are also major products as shown
388 in Fig. 3a, suggesting that GECKO-A simulated n-alkane oxidation very well. There are notable
389 differences in molecular composition for SOA simulated by CP compared to tgBoost (Fig. A2):
390 the major compounds are 1st generation single and multi-functionalized products, followed by
391 some 2nd and 3rd generation products, without decomposition products in the top species.

392 The simulated T_g by both methods for each compound are listed in Fig. 3. Overall
393 tgBoost predicts T_g values between 157 – 221 K which are much lower compared to CP,
394 especially with significant differences for organic nitrates and multi-functionalized species. As
395 tgBoost considers the molecular structure, functional group and atomic interconnectivity of a
396 molecule, it should make better predictions for multi-functionalized compounds based on the
397 presence of different functional groups. CP is based on elemental composition and it predicts
398 high T_g for compounds with high molar mass, predicting same T_g for isomers. In addition, the
399 CP for CHON compounds was developed based on T_g values mainly estimated from their
400 melting points, as there are limited number of CHON compounds with measured T_g available.
401 T_g of organic nitrates are especially scarce and future T_g measurements for organic nitrates are
402 desired to improve T_g parameterizations. For these reasons, CP overestimates T_g for oxidation
403 products of n-alkane with long chain on average by ~66 K compared to tgBoost, overpredicting
404 SOA viscosity as shown in Fig. 2(a).

405 Figure 3 also lists α_{eff} values, showing that they are very close to 1 for tgBoost, with
406 SOA to be low viscous liquid with little kinetic limitations in mass accommodation. Additional
407 oxidation products with lower concentrations are listed in Fig. A3 and their α_{eff} remain also
408 close to 1. In contrast, as CP predicts the SOA phase state to be viscous amorphous semisolid,
409 α_{eff} values for semi-volatile compounds become significantly smaller to kinetically limit mass
410 accommodation. This decrease of α_{eff} is larger for compounds with higher volatility, as such
411 compounds have higher re-evaporation rate on viscous particles with lower rate of bulk
412 diffusion (Shiraiwa and Pöschl, 2021) (Fig. A3). α_{eff} for lower volatility compounds remain
413 high, as they exhibit much lower desorption rates and are less likely to re-evaporate, even if
414 their diffusion into the bulk is slow. Consequently, SOA simulated with CP mainly consists of
415 later generation products with higher functionalization and molar masses.

416 Figure 3(b) shows top 15 oxidation products of n-decane (C₁₀H₂₆) as predicted by
417 GECKO-A with tgBoost. SOA is mostly composed of 2nd and 3rd generation products with

418 multiple functional groups including nitrates, ketones, and alcohols. These highly oxidized
419 products have T_g in the range of 225 – 304 K, with similar predictions by CP and tgBoost. This
420 is consistent with previous studies that demonstrated successful applications of CP to predict
421 the measured viscosity of SOA derived from biogenic and other relatively small precursors
422 (DeRieux et al., 2018; Smith et al., 2021; Baboornian et al., 2022). These results are consistent
423 with total ion thermal desorption profiles of n-alkane SOA formed in the presence of NO_x (Lim
424 and Ziemann, 2009b): C₁₀ SOA was observed to have a broad single peak around ~75 °C,
425 indicating the presence of low volatility multigenerational products; in contrast, C₁₂ and C₁₅
426 SOA exhibited two peaks with one larger peak at lower temperature, corresponding to 1st
427 generation products and another smaller peak for multigenerational products. The phase state
428 of n-decane SOA is predicted to be semisolid, but kinetic limitations are not strong as α_{eff} values
429 for most compounds are only slightly reduced from 1.

430

431 **Effects of mass loadings on viscosity.**

432 The use of higher mass loadings in chamber experiments than ambient conditions
433 assured that the condensation of semi-volatile vapors to suspended particles is a dominant
434 process over vapor wall deposition (Zhang et al., 2014; Matsunaga and Ziemann, 2010).
435 Chamber experiments of n-alkane photooxidation at high NO_x were also conducted with lower
436 mass loading by Presto et al. (2010), who measured temporal evolution of SOA yields as shown
437 in Fig. 4(a). SOA yields are increased with an increase of SOA mass concentrations, which is
438 consistent with SOA absorptive partitioning theory (Pankow, 1994). The oxidation of larger
439 precursors leads to higher SOA yields, in agreement with Lim and Ziemann (2009b) as
440 presented in Fig. 1a. As shown with solid lines, the GECKO-A box model simulated
441 experimental observations of SOA yields very well.

442 Figure 4(b) depicts the simulated SOA viscosity. We observed the same trend as Fig.
443 2(a) with lowering of viscosity upon an increase of carbon number n . SOA phase state is
444 predicted to be semisolid for low carbon n , while it is expected to be liquid for high n . The
445 predicted viscosity is about one order of magnitude higher compared to Fig. 2(a). Lower mass
446 loadings suppress partitioning of higher volatility compounds, resulting in higher viscosity as
447 condensation would be dominated by lower volatility compounds with higher T_g (Jain et al.,
448 2018; Champion et al., 2019; Grayson et al., 2016; DeRieux et al., 2018).

449

450 **Atmospheric Implications.**

451 The phase state and viscosity of SOA formed by IVOCs have been largely unknown
452 and unexplored. We demonstrated in this study that SOA derived from small and middle size
453 n-alkanes (C₁₂ and smaller) mostly consists of multigenerational oxidation products to adopt an
454 amorphous semisolid state, while larger n-alkane SOA are mainly composed of first generation
455 lightly oxidized products with one or two functional groups to adopt a low viscous liquid state.
456 This result is counter-intuitive, as it has been established that higher molar mass would lead to
457 higher glass transition temperature, and hence, higher viscosity (Koop et al., 2011; Shiraiwa et
458 al., 2017). In fact, the viscosity of biogenic SOA follows this trend: the viscosity of isoprene
459 (C₅H₈) SOA is reported to be lower than monoterpene (C₁₀H₁₆, such as α -pinene and limonene)
460 SOA (Renbaum-Wolff et al., 2013; Zhang et al., 2019), while oxidation products of
461 sesquiterpene (C₁₅H₂₄) increase viscosity of SOA (Smith et al., 2021), which is captured by
462 empirical parameterizations based on elemental composition (DeRieux et al., 2018; Li et al.,
463 2020). In contrast, n-alkane SOA exhibits an opposite trend, as indicated by thermal desorption
464 measurements that show that DOS in SOA formed by oxidation of large n-alkanes has higher
465 volatility. Hence, the SOA has lower viscosity, due to the enhanced presence of less
466 functionalized first-generation products (Li et al., 2020; Zhang et al., 2019). This trend is
467 successfully predicted by GECKO-A combined with machine learning-based model tgBoost,
468 which emphasizes the importance of consideration of functionality and molecular structure in
469 accurate predictions of T_g . The relationship between viscosity and composition is also reflected
470 in the atomic O:C and N:C ratios of n-alkane SOA, which decrease monotonically upon an
471 increase of carbon number of the n-alkane, since higher oxidation state and functionalization
472 can increase T_g (DeRieux et al., 2018; Koop et al., 2011; Shiraiwa et al., 2017; Saukko et al.,
473 2012).

474 IVOCs have gained growing attention for better characterization of urban air quality, as
475 they represent an important source of SOA as shown by chamber experiments (Aimanant and
476 Ziemann, 2013a; Lim and Ziemann, 2009b) and as observed in field observations (Gentner et
477 al., 2012; Li et al., 2022; Robinson et al., 2007; McDonald et al., 2018). While a few large-scale
478 aerosol models treat IVOC SOA to achieve better agreement with ambient measurements (de
479 Gouw et al., 2011; Li et al., 2022; Zhao et al., 2016), IVOC SOA is still highly uncertain in
480 terms of chemical composition and particle phase state and model parameters and treatments
481 for SOA formation and partitioning are poorly constrained. Our study provides critical insights
482 for these aspects, showing that n-alkane SOA formation under high NO_x conditions (as usually
483 the case for ambient urban air) is dominated by gas-phase chemistry followed by partitioning.
484 As the generated SOA particles adopt a low viscous state, there is little kinetic limitations of

485 mass accommodation and bulk diffusion, which supports the application of equilibrium SOA
486 partitioning in the boundary layer. While the experiments and modeling were conducted for dry
487 conditions in this study, the phase state and viscosity of ambient n-alkane SOA would be
488 expected to be even lower under humid conditions due to hygroscopic growth and water acting
489 as plasticizer. Note that further experiments and model simulations are required for different
490 conditions for middle and upper free troposphere, as viscosity is expected to become higher
491 under low temperatures.

492 It is **notable** that the combination of tgBoost and GECKO-A box model **successfully**
493 simulates SOA yields, functional group distributions and phase state. This new model
494 represents a unique and comprehensive tool for simulating formation, partitioning and chemical
495 evolution of SOA, opening up a new avenue for analyzing complex interplay of gas-phase
496 chemistry and particle-phase processes and composition in SOA for detailed analysis and
497 interpretation of laboratory experiments and field observations. In addition, we propose to
498 pursue the application of this model as a basis for the development of a detailed master
499 mechanism of multiphase aerosol chemistry as well as for the derivation of simplified but
500 realistic parameterizations for air quality and climate models. In regional and global air quality
501 models, it is challenging and computationally very expensive to treat complex SOA multiphase
502 processes. Thus, such processes should be treated in efficient but effective way and the new
503 model shall serve as benchmark for the development of simplified SOA descriptions.

504

505

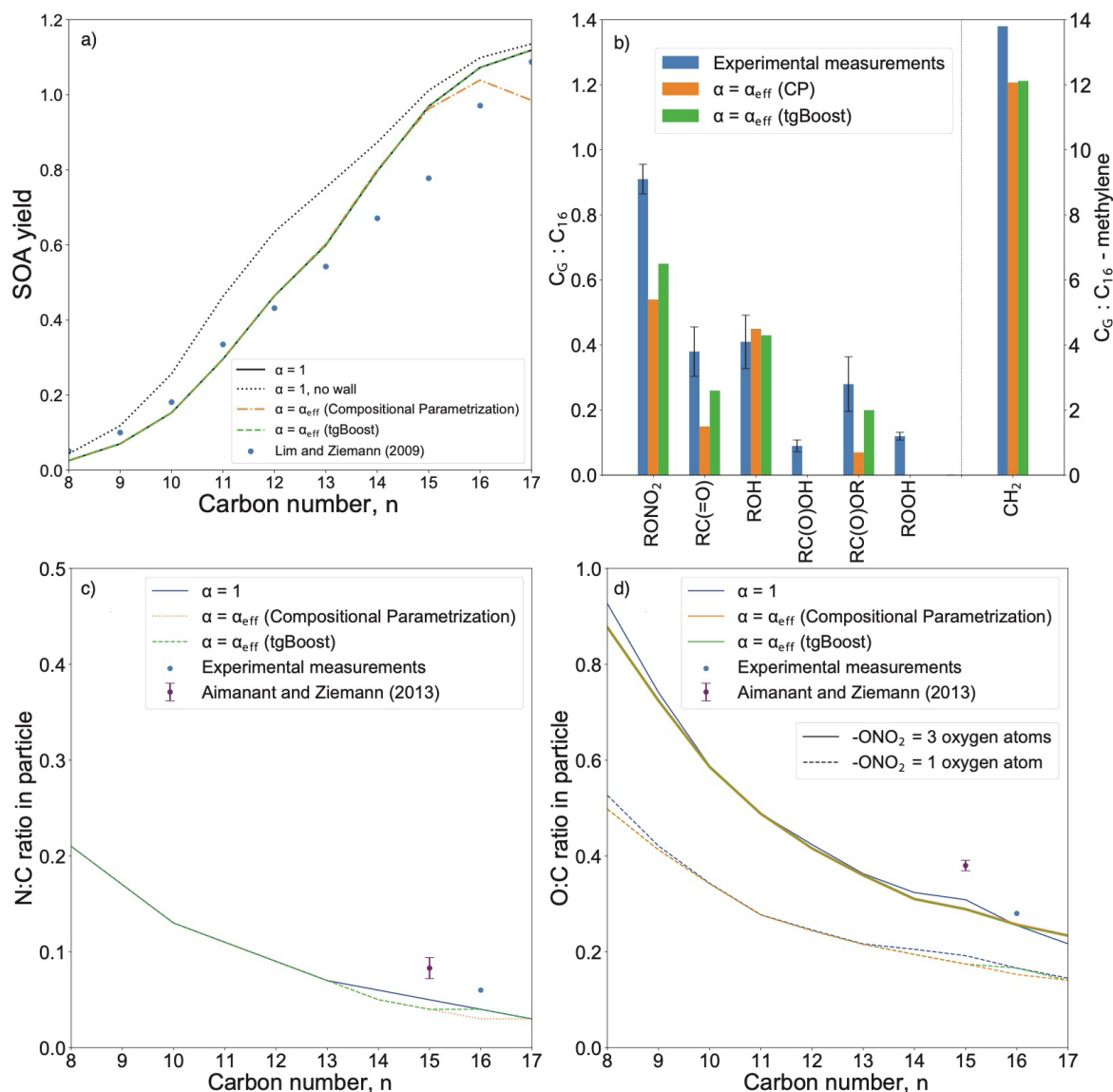
506 **Acknowledgements.** This work was also funded by U.S. Department of Energy (DE-
507 SC0018349), U.S. National Science Foundation (AGS-1654104) and the Campus France
508 (Make Our Planet Great Again short stay program grant, mopga-short-0000000116). In
509 addition, PZ acknowledges support from the National Science Foundation under grant AGS-
510 1750447.

511

512 **Authors contributions.** TG and MS designed the study. TG conducted model simulations and
513 data analysis. RV, MC, and BA developed the GECKO-A model. YL and PZ conducted
514 experimental measurements. All authors discussed the results. TG and MS wrote the manuscript
515 with contributions from all coauthors.

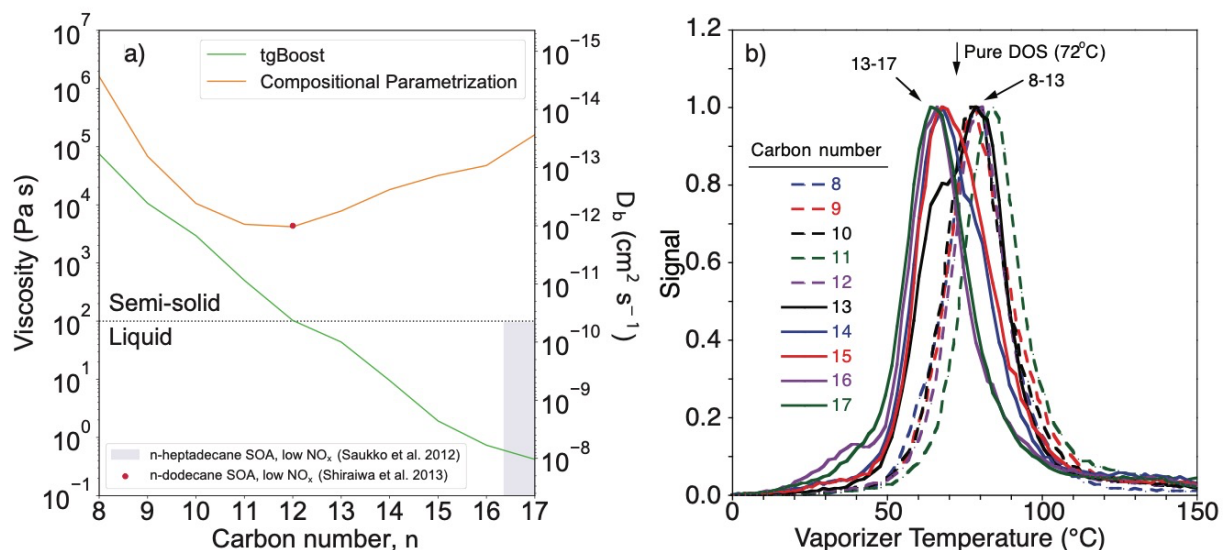
516 **Competing interests.** At least one of the (co-)authors is a member of the editorial board of
517 Atmospheric Chemistry and Physics.

518 **Code/Data availability.** The simulation data may be obtained from the corresponding author
519 upon request. The model tgBoost is available in Github (<https://github.com/U0M0Z/tgpipe>) and
520 in the homepage (<https://azothai.ps.uci.edu/>).
521



522

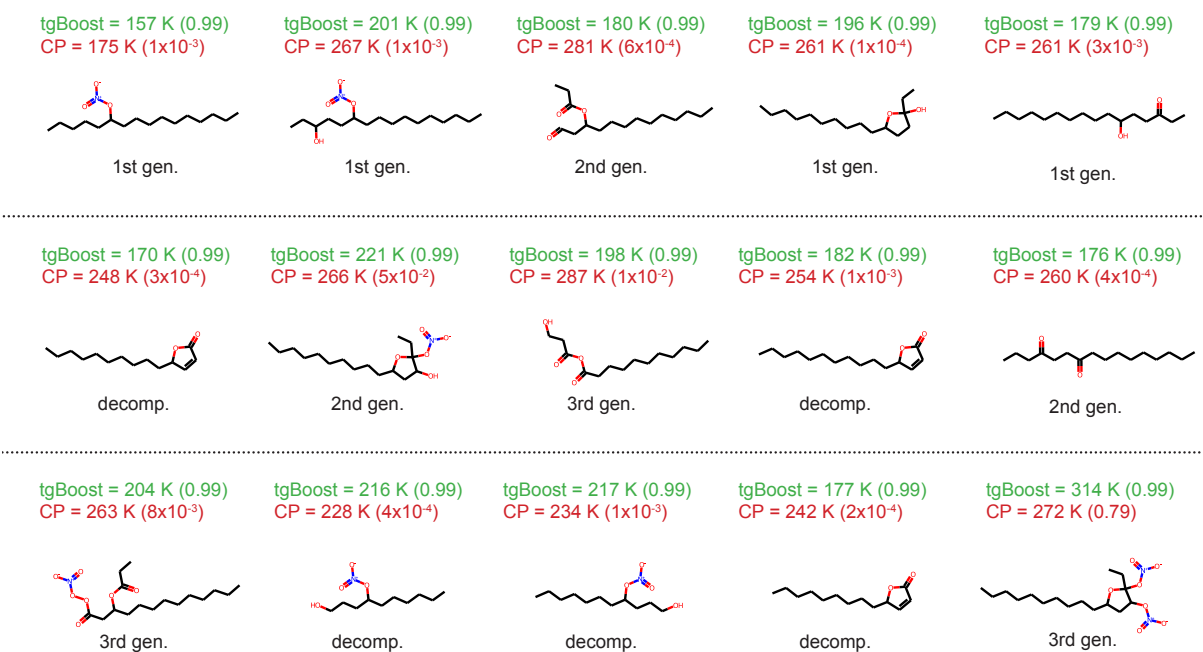
523 **Figure 1:** (a) Yields of SOA generated from OH oxidation of linear n-alkanes as measured by
 524 Lim and Ziemann (2009) (markers) (Lim and Ziemann, 2009b) and modeled by the GECKO-
 525 A box model (lines). The black line represents the base case with mass accommodation
 526 coefficient (α) of 1. The dashed lines represent simulations with effective mass accommodation
 527 coefficient (α_{eff}) as a function of bulk diffusivity from tgBoost (green) and the compositional
 528 parameterization (orange). (b) Simulated functional group distributions of n-hexadecane
 529 ($C_{16}H_{34}$) oxidation products in the particle phase. The blue bars represent experimental
 530 measurements. The green and orange bars represent GECKO-A box model simulations with
 531 α_{eff} with tgBoost and the compositional parameterization, respectively. (c) N:C and (d) O:C
 532 ratios in SOA formed by n-alkane oxidation simulated by the GECKO-A box model. The black
 533 line represents the base case with α of 1. The dashed lines represent simulations with α_{eff} with
 534 tgBoost (green) and the compositional parameterization (orange).



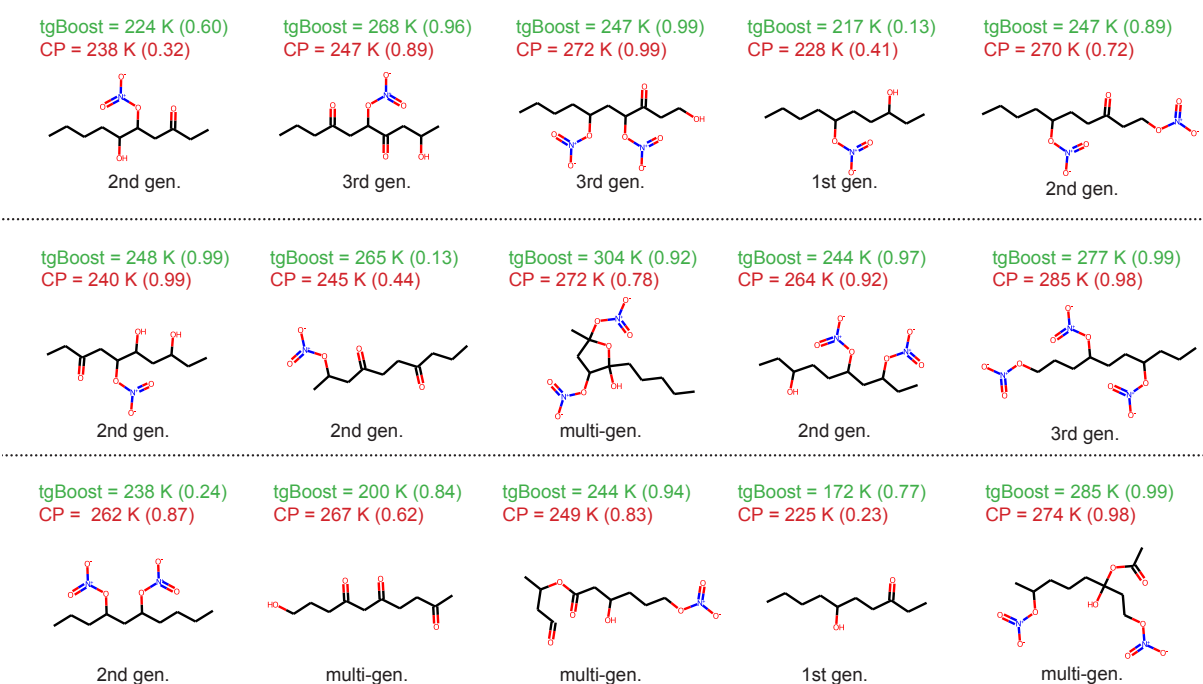
535

536 **Figure 2:** Phase state of n-alkane SOA. (a) Predicted viscosity of SOA generated from n-
 537 alkanes as computed by the GECKO-A box model with the T_g compositional parametrization
 538 (orange line) and tgBoost (green line) at the last step of the simulations ($t = 3600$ s). (b) Thermal
 539 desorption temperatures of dioctyl sebacate (DOS) that was present as seed particles in n-alkane
 540 SOA.

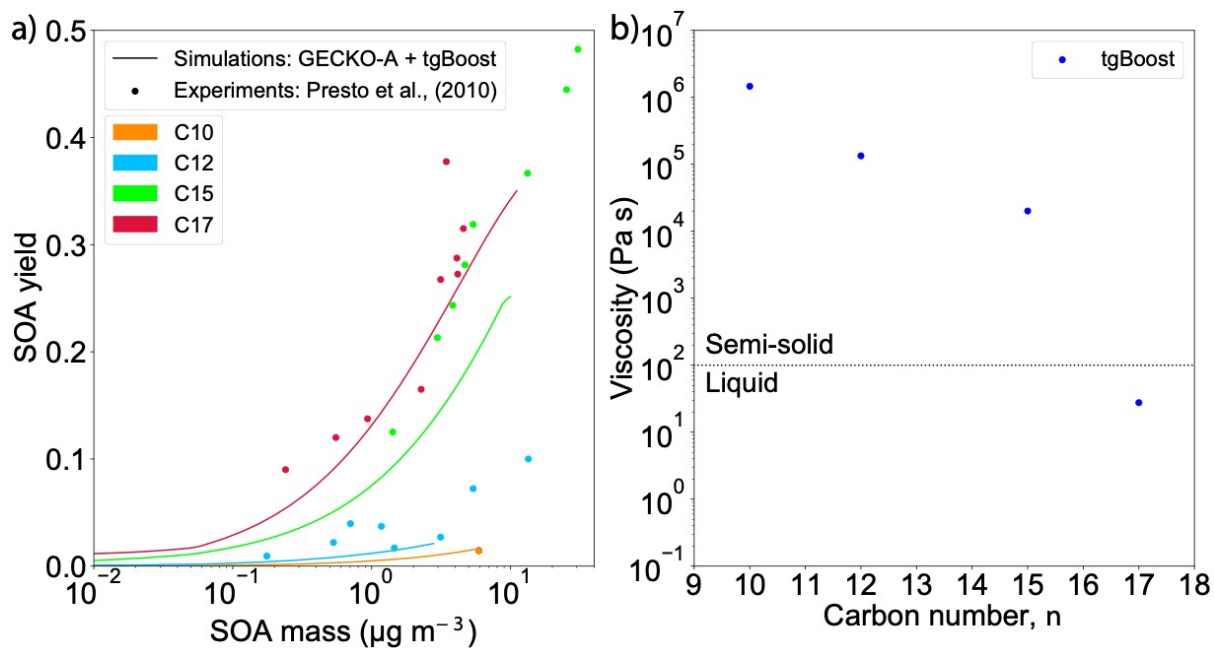
(a) n-Hexadecane (C16)



(b) n-Decane (C10)



541
 542 **Figure 3:** Molecular composition of oxidation products of n-alkanes under high NOx
 543 conditions in the particle phase. Top 15 SOA contributors with highest concentrations in (a) n-
 544 Hexadecane (C₁₆H₃₄) SOA and (b) n-Decane (C₁₀H₂₂) simulated by GECKO-A with effective
 545 mass accommodation coefficient (α_{eff}) with tgBoost. The species are reported in descending
 546 concentrations from left to right and from top to bottom. Positional isomers are lumped into
 547 one species. Listed values are T_g as calculated by tgBoost and CP and α_{eff} values at the end of
 548 simulation (3600 s) in brackets. Types of compounds are also noted (1st, 2nd, and 3rd generation
 549 products, decomposition products).



550
 551
 552
 553
 554
 555
 556
 557

Figure 4: Effects of mass loadings on SOA yields and viscosity. (a) SOA yields from photo-oxidation of n-decane (C10), n-dodecane (C12), n-pentadecane (C15), and n-heptadecane (C17) at high NO_x as a function of SOA mass concentration, as measured in Presto et al. (2010) (markers) and as modeled by the GECKO-A box model combined with tgBoost (lines). (b) SOA viscosity as modeled by the GECKO-A box model combined with tgBoost.

558 **References.**

- 559 Aimanant, S. and Ziemann, P. J.: Chemical Mechanisms of Aging of Aerosol Formed from the
560 Reaction of n-Pentadecane with OH Radicals in the Presence of NO_x, *Aerosol Sci. Technol.*,
561 47, 979-990, 10.1080/02786826.2013.804621, 2013a.
- 562 Aimanant, S. and Ziemann, P. J.: Development of Spectrophotometric Methods for the Analysis
563 of Functional Groups in Oxidized Organic Aerosol, *Aerosol Sci. Technol.*, 47, 581-591,
564 10.1080/02786826.2013.773579, 2013b.
- 565 Atkinson, R., Carter, W. P. L., Winer, A. M., and Pitts, J. N.: An Experimental Protocol for the
566 Determination of OH Radical Rate Constants with Organics Using Methyl Nitrite Photolysis
567 as an OH Radical Source, *Journal of the Air Pollution Control Association*, 31, 1090-1092,
568 10.1080/00022470.1981.10465331, 1981.
- 569 Aumont, B., Szopa, S., and Madronich, S.: Modelling the evolution of organic carbon during
570 its gas-phase tropospheric oxidation: development of an explicit model based on a self
571 generating approach, *Atmospheric Chemistry and Physics*, 5, 2497-2517, 10.5194/acp-5-2497-
572 2005, 2005.
- 573 Aumont, B., Valorso, R., Mouchel-Vallon, C., Camredon, M., Lee-Taylor, J., and Madronich,
574 S.: Modeling SOA formation from the oxidation of intermediate volatility n-alkanes,
575 *Atmospheric Chemistry and Physics*, 12, 7577-7589, 10.5194/acp-12-7577-2012, 2012.
- 576 Aumont, B., Camredon, M., Mouchel-Vallon, C., La, S., Ouzebidou, F., Valorso, R., Lee-
577 Taylor, J., and Madronich, S.: Modeling the influence of alkane molecular structure on
578 secondary organic aerosol formation, *Faraday Discussions*, 165, 105-122,
579 10.1039/C3FD00029J, 2013.
- 580 Baboornian, V. J., Crescenzo, G. V., Huang, Y., Mahrt, F., Shiraiwa, M., Bertram, A. K., and
581 Nizkorodov, S. A.: Sunlight can convert atmospheric aerosols into a glassy solid state and
582 modify their environmental impacts, *Proc. Nat. Acad. Sci.*, 119, e2208121119,
583 10.1073/pnas.2208121119, 2022.
- 584 Bakker-Arkema, J. G. and Ziemann, P. J.: Minimizing Errors in Measured Yields of Particle-
585 Phase Products Formed in Environmental Chamber Reactions: Revisiting the Yields of β -
586 Hydroxynitrates Formed from 1-Alkene + OH/NO_x Reactions, *ACS Earth and Space*
587 *Chemistry*, 5, 690-702, 10.1021/acsearthspacechem.1c00008, 2021.
- 588 Champion, W. M., Rothfuss, N. E., Petters, M. D., and Grieshop, A. P.: Volatility and Viscosity
589 Are Correlated in Terpene Secondary Organic Aerosol Formed in a Flow Reactor,
590 *Environmental Science & Technology Letters*, 6, 513-519, 10.1021/acs.estlett.9b00412, 2019.
- 591 de Gouw, J. A., Middlebrook, A. M., Warneke, C., Ahmadov, R., Atlas, E. L., Bahreini, R.,
592 Blake, D. R., Brock, C. A., Brioude, J., Fahey, D. W., Fehsenfeld, F. C., Holloway, J. S., Le
593 Henaff, M., Lueb, R. A., McKeen, S. A., Meagher, J. F., Murphy, D. M., Paris, C., Parrish, D.
594 D., Perring, A. E., Pollack, I. B., Ravishankara, A. R., Robinson, A. L., Ryerson, T. B.,
595 Schwarz, J. P., Spackman, J. R., Srinivasan, A., and Watts, L. A.: Organic Aerosol Formation
596 Downwind from the Deepwater Horizon Oil Spill, *Science*, 331, 1295-1299,
597 10.1126/science.1200320, 2011.

598 DeRieux, W. S. W., Li, Y., Lin, P., Laskin, J., Laskin, A., Bertram, A. K., Nizkorodov, S. A.,
599 and Shiraiwa, M.: Predicting the glass transition temperature and viscosity of secondary organic
600 material using molecular composition, *Atmos. Chem. Phys.*, 18, 6331-6351, 10.5194/acp-18-
601 6331-2018, 2018.

602 Dette, H. P., Qi, M., Schröder, D. C., Godt, A., and Koop, T.: Glass-forming properties of 3-
603 Methylbutane-1,2,3-tricarboxylic acid and its mixtures with water and pinonic acid, *The*
604 *Journal of Physical Chemistry A*, 118, 7024-7033, 10.1021/jp505910w, 2014.

605 Docherty, K. S., Wu, W., Lim, Y. B., and Ziemann, P. J.: Contributions of organic peroxides
606 to secondary aerosol formed from reactions of monoterpenes with O₃, *Environ. Sci. Technol.*,
607 39, 4049-4059, 10.1021/es050228s, 2005.

608 Evoy, E., Maclean, A. M., Rovelli, G., Li, Y., Tsimpidi, A. P., Karydis, V. A., Kamal, S.,
609 Lelieveld, J., Shiraiwa, M., Reid, J. P., and Bertram, A. K.: Predictions of diffusion rates of
610 large organic molecules in secondary organic aerosols using the Stokes–Einstein and fractional
611 Stokes–Einstein relations, *Atmos. Chem. Phys.*, 19, 10073-10085, 10.5194/acp-19-10073-
612 2019, 2019.

613 Farmer, D. K., Matsunaga, A., Docherty, K. S., Surratt, J. D., Seinfeld, J. H., Ziemann, P. J.,
614 and Jimenez, J. L.: Response of an aerosol mass spectrometer to organonitrates and
615 organosulfates and implications for atmospheric chemistry, *Proc. Nat. Acad. Sci.*, 107, 6670-
616 6675, 2010.

617 Galeazzo, T. and Shiraiwa, M.: Predicting glass transition temperature and melting point of
618 organic compounds via machine learning and molecular embeddings, *Environmental Science:*
619 *Atmospheres*, 2, 362-374, 10.1039/D1EA00090J, 2022.

620 Galeazzo, T., Valorso, R., Li, Y., Camredon, M., Aumont, B., and Shiraiwa, M.: Estimation of
621 secondary organic aerosol viscosity from explicit modeling of gas-phase oxidation of isoprene
622 and α -pinene, *Atmos. Chem. Phys.*, 21, 10199-10213, 10.5194/acp-21-10199-2021, 2021.

623 Gentner, D. R., Isaacman, G., Worton, D. R., Chan, A. W. H., Dallmann, T. R., Davis, L., Liu,
624 S., Day, D. A., Russell, L. M., Wilson, K. R., Weber, R., Guha, A., Harley, R. A., and Goldstein,
625 A. H.: Elucidating secondary organic aerosol from diesel and gasoline vehicles through detailed
626 characterization of organic carbon emissions, *Proc. Nat. Acad. Sci.*, 109, 18318-18323,
627 10.1073/pnas.1212272109, 2012.

628 Grayson, J. W., Zhang, Y., Mutzel, A., Renbaum-Wolff, L., Böge, O., Kamal, S., Herrmann,
629 H., Martin, S. T., and Bertram, A. K.: Effect of varying experimental conditions on the viscosity
630 of α -pinene derived secondary organic material, *Atmos. Chem. Phys.*, 16, 6027-6040,
631 10.5194/acp-16-6027-2016, 2016.

632 Grayson, J. W., Evoy, E., Song, M., Chu, Y., Maclean, A., Nguyen, A., Upshur, M. A.,
633 Ebrahimi, M., Chan, C. K., Geiger, F. M., Thomson, R. J., and Bertram, A. K.: The effect of
634 hydroxyl functional groups and molar mass on the viscosity of non-crystalline organic and
635 organic–water particles, *Atmos. Chem. Phys.*, 17, 8509-8524, 10.5194/acp-17-8509-2017,
636 2017.

637 Jain, S., Fischer, B. K., and Petrucci, A. G.: The Influence of Absolute Mass Loading of
638 Secondary Organic Aerosols on Their Phase State, *Atmosphere*, 9, 10.3390/atmos9040131,
639 2018.

640 Jenkin, M. E., Valorso, R., Aumont, B., and Rickard, A. R.: Estimation of rate coefficients and
641 branching ratios for reactions of organic peroxy radicals for use in automated mechanism
642 construction, *Atmos. Chem. Phys.*, 19, 7691-7717, 10.5194/acp-19-7691-2019, 2019.

643 Jenkin, M. E., Valorso, R., Aumont, B., Rickard, A. R., and Wallington, T. J.: Estimation of
644 rate coefficients and branching ratios for gas-phase reactions of OH with aliphatic organic
645 compounds for use in automated mechanism construction, *Atmos. Chem. Phys.*, 18, 9297-9328,
646 10.5194/acp-18-9297-2018, 2018a.

647 Jenkin, M. E., Valorso, R., Aumont, B., Rickard, A. R., and Wallington, T. J.: Estimation of
648 rate coefficients and branching ratios for gas-phase reactions of OH with aromatic organic
649 compounds for use in automated mechanism construction, *Atmos. Chem. Phys.*, 18, 9329-9349,
650 10.5194/acp-18-9329-2018, 2018b.

651 Jimenez, J. L., Canagaratna, M. R., Donahue, N. M., Prevot, A. S. H., Zhang, Q., Kroll, J. H.,
652 DeCarlo, P. F., Allan, J. D., Coe, H., Ng, N. L., Aiken, A. C., Docherty, K. S., Ulbrich, I. M.,
653 Grieshop, A. P., Robinson, A. L., Duplissy, J., Smith, J. D., Wilson, K. R., Lanz, V. A., Hueglin,
654 C., Sun, Y. L., Tian, J., Laaksonen, A., Raatikainen, T., Rautiainen, J., Vaattovaara, P., Ehn,
655 M., Kulmala, M., Tomlinson, J. M., Collins, D. R., Cubison, M. J., Dunlea, E. J., Huffman, J.
656 A., Onasch, T. B., Alfarra, M. R., Williams, P. I., Bower, K., Kondo, Y., Schneider, J.,
657 Drewnick, F., Borrmann, S., Weimer, S., Demerjian, K., Salcedo, D., Cottrell, L., Griffin, R.,
658 Takami, A., Miyoshi, T., Hatakeyama, S., Shimono, A., Sun, J. Y., Zhang, Y. M., Dzepina, K.,
659 Kimmel, J. R., Sueper, D., Jayne, J. T., Herndon, S. C., Trimborn, A. M., Williams, L. R.,
660 Wood, E. C., Middlebrook, A. M., Kolb, C. E., Baltensperger, U., and Worsnop, D. R.:
661 Evolution of organic aerosols in the atmosphere, *Science*, 326, 1525-1529,
662 10.1126/science.1180353, 2009.

663 Julin, J., Winkler, P. M., Donahue, N. M., Wagner, P. E., and Riipinen, I. A.: Near unity mass
664 accommodation coefficient of organic molecules of varying structure, *Environ. Sci. Technol.*,
665 48, 12083–12089, 10.1021/es501816h, 2014.

666 Knopf, D. A. and Alpert, P. A.: Atmospheric ice nucleation, *Nat. Rev. Phys.*, 5, 203-217,
667 10.1038/s42254-023-00570-7, 2023.

668 Koop, T., Bookhold, J., Shiraiwa, M., and Pöschl, U.: Glass transition and phase state of organic
669 compounds: dependency on molecular properties and implications for secondary organic
670 aerosols in the atmosphere, *Physical Chemistry Chemical Physics*, 13, 19238-19255, 2011.

671 Krechmer, J. E., Pagonis, D., Ziemann, P. J., and Jimenez, J. L.: Quantification of gas-wall
672 partitioning in Teflon environmental chambers using rapid bursts of low-volatility oxidized
673 species generated in situ, *Environ. Sci. Technol.*, 50, 5757-5765, 2016.

674 Kroll, J. H. and Seinfeld, J. H.: Chemistry of secondary organic aerosol: Formation and
675 evolution of low-volatility organics in the atmosphere, *Atmos. Environ.*, 42, 3593-3624,
676 10.1016/j.atmosenv.2008.01.003, 2008.

677 La, Y. S., Camredon, M., Ziemann, P. J., Valorso, R., Matsunaga, A., Lannuque, V., Lee-
678 Taylor, J., Hodzic, A., Madronich, S., and Aumont, B.: Impact of chamber wall loss of gaseous
679 organic compounds on secondary organic aerosol formation: explicit modeling of SOA
680 formation from alkane and alkene oxidation, *Atmospheric Chemistry and Physics*, 16, 1417-
681 1431, 10.5194/acp-16-1417-2016, 2016.

682 Li, J. L., Li, K., Li, H., Wang, X. Z., Wang, W. G., Wang, K., and Ge, M. F.: Long-chain
683 alkanes in the atmosphere: A review *, *J. Environ. Sci.*, 114, 37-52, 10.1016/j.jes.2021.07.021,
684 2022.

685 Li, Y., Day, D. A., Stark, H., Jimenez, J. L., and Shiraiwa, M.: Predictions of the glass transition
686 temperature and viscosity of organic aerosols from volatility distributions, *Atmos. Chem. Phys.*,
687 20, 8103-8122, 10.5194/acp-20-8103-2020, 2020.

688 Lim, Y. B. and Ziemann, P. J.: Chemistry of Secondary Organic Aerosol Formation from OH
689 Radical-Initiated Reactions of Linear, Branched, and Cyclic Alkanes in the Presence of NO_x,
690 *Aerosol Sci. Technol.*, 43, 604-619, 10.1080/02786820902802567, 2009a.

691 Lim, Y. B. and Ziemann, P. J.: Effects of Molecular Structure on Aerosol Yields from OH
692 Radical-Initiated Reactions of Linear, Branched, and Cyclic Alkanes in the Presence of NO_x,
693 *Environ. Sci. Technol.*, 43, 2328-2334, 10.1021/es803389s, 2009b.

694 Maclean, A. M., Smith, N. R., Li, Y., Huang, Y., Hettiyadura, A. P. S., Crescenzo, G. V.,
695 Shiraiwa, M., Laskin, A., Nizkorodov, S. A., and Bertram, A. K.: Humidity-Dependent
696 Viscosity of Secondary Organic Aerosol from Ozonolysis of β -Caryophyllene: Measurements,
697 Predictions, and Implications, *ACS Earth and Space Chemistry*, 5, 305-318,
698 10.1021/acsearthspacechem.0c00296, 2021.

699 Matsunaga, A. and Ziemann, P. J.: Gas-wall partitioning of organic compounds in a Teflon film
700 chamber and potential effects on reaction product and aerosol yield measurements, *Aerosol Sci.*
701 *Technol.*, 44, 881-892, 10.1080/02786826.2010.501044, 2010.

702 McDonald, B. C., de Gouw, J. A., Gilman, J. B., Jathar, S. H., Akherati, A., Cappa, C. D.,
703 Jimenez, J. L., Lee-Taylor, J., Hayes, P. L., McKeen, S. A., Cui, Y. Y., Kim, S.-W., Gentner,
704 D. R., Isaacman-VanWertz, G., Goldstein, A. H., Harley, R. A., Frost, G. J., Roberts, J. M.,
705 Ryerson, T. B., and Trainer, M.: Volatile chemical products emerging as largest petrochemical
706 source of urban organic emissions, *Science*, 359, 760, 2018.

707 Mu, Q., Shiraiwa, M., Octaviani, M., Ma, N., Ding, A., Su, H., Lammel, G., Pöschl, U., and
708 Cheng, Y.: Temperature effect on phase state and reactivity controls atmospheric multiphase
709 chemistry and transport of PAHs, *Science Advances*, 4, eaap7314, 2018.

710 Nannoolal, Y., Rarey, J., and Ramjugernath, D.: Estimation of pure component properties - Part
711 3. Estimation of the vapor pressure of non-electrolyte organic compounds via group
712 contributions and group interactions, *Fluid Phase Equilibria*, 269, 117-133,
713 10.1016/j.fluid.2008.04.020, 2008.

714 O'Brien, R. E., Li, Y., Kiland, K. J., Katz, E. F., Or, V. W., Legaard, E., Walhout, E. Q.,
715 Thrasher, C., Grassian, V. H., DeCarlo, P. F., Bertram, A. K., and Shiraiwa, M.: Emerging
716 investigator series: chemical and physical properties of organic mixtures on indoor surfaces
717 during HOMEChem, *Environmental Science: Processes & Impacts*, 23, 559-568,
718 10.1039/D1EM00060H, 2021.

719 Pankow, J. F.: An absorption-model of the gas aerosol partitioning involved in the formation
720 of secondary organic aerosol, *Atmos. Environ.*, 28, 189-193, 1994.

- 721 Petters, S. S., Kreidenweis, S. M., Grieshop, A. P., Ziemann, P. J., and Petters, M. D.:
722 Temperature- and Humidity-Dependent Phase States of Secondary Organic Aerosols,
723 *Geophysical Research Letters*, 46, 1005-1013, 10.1029/2018GL080563, 2019.
- 724 Pöschl, U. and Shiraiwa, M.: Multiphase Chemistry at the Atmosphere–Biosphere Interface
725 Influencing Climate and Public Health in the Anthropocene, *Chemical Reviews*, 115, 4440–
726 4475, 10.1021/cr500487s, 2015.
- 727 Praske, E., Otkjær, R. V., Crouse, J. D., Hethcox, J. C., Stoltz, B. M., Kjaergaard, H. G., and
728 Wennberg, P. O.: Atmospheric autoxidation is increasingly important in urban and suburban
729 North America, *Proc. Nat. Acad. Sci.*, 115, 64-69, 10.1073/pnas.1715540115, 2018.
- 730 Presto, A. A., Miracolo, M. A., Donahue, N. M., and Robinson, A. L.: Secondary organic
731 aerosol formation from high-NO_x photo-oxidation of low volatility precursors: n-alkanes,
732 *Environ. Sci. Technol.*, 44, 2029-2034, 10.1021/es903712r, 2010.
- 733 Pye, H. O. T., D’Ambro, E. L., Lee, B. H., Schobesberger, S., Takeuchi, M., Zhao, Y., Lopez-
734 Hilfiker, F., Liu, J., Shilling, J. E., Xing, J., Mathur, R., Middlebrook, A. M., Liao, J., Welti,
735 A., Graus, M., Warneke, C., de Gouw, J. A., Holloway, J. S., Ryerson, T. B., Pollack, I. B., and
736 Thornton, J. A.: Anthropogenic enhancements to production of highly oxygenated molecules
737 from autoxidation, *Proc. Nat. Acad. Sci.*, 116, 6641, 10.1073/pnas.1810774116, 2019.
- 738 Ranney, A. P., Longnecker, E. R., Ziola, A. C., and Ziemann, P. J.: Measured and Modeled
739 Secondary Organic Aerosol Products and Yields from the Reaction of n-Hexadecane +
740 OH/NO_x, *ACS Earth and Space Chemistry*, 7, 2298-2310,
741 10.1021/acsearthspacechem.3c00227, 2023.
- 742 Reid, J. P., Bertram, A. K., Topping, D. O., Laskin, A., Martin, S. T., Petters, M. D., Pope, F.
743 D., and Rovelli, G.: The viscosity of atmospherically relevant organic particles, *Nature*
744 *Communications*, 9, 956, 10.1038/s41467-018-03027-z, 2018.
- 745 Renbaum-Wolff, L., Grayson, J. W., Bateman, A. P., Kuwata, K., Sellier, M., Murray, B. J.,
746 Schilling, J. E., Martin, S. T., and Bertram, A. K.: Viscosity of α -pinene secondary organic
747 material and implications for particle growth and reactivity, *Proceedings of the National*
748 *Academy of Sciences of the United States of America*, 110, 8014-8019,
749 10.1073/pnas.1219548110 2013.
- 750 Robinson, A. L., Donahue, N. M., Shrivastava, M. K., Weitkamp, E. A., Sage, A. M., Grieshop,
751 A. P., Lane, T. E., Pierce, J. R., and Pandis, S. N.: Rethinking organic aerosols: Semivolatile
752 emissions and photochemical aging, *Science*, 315, 1259-1262, 10.1126/science.1133061, 2007.
- 753 Rothfuss, N. E. and Petters, M. D.: Influence of Functional Groups on the Viscosity of Organic
754 Aerosol, *Environ. Sci. Technol.*, 51, 271-279, 10.1021/acs.est.6b04478, 2017.
- 755 Saukko, E., Lambe, A. T., Massoli, P., Koop, T., Wright, J. P., Croasdale, D. R., Pedernera, D.
756 A., Onasch, T. B., Laaksonen, A., Davidovits, P., Worsnop, D. R., and Virtanen, A.: Humidity-
757 dependent phase state of SOA particles from biogenic and anthropogenic precursors,
758 *Atmospheric Chemistry and Physics*, 12, 7517-7529, 10.5194/acp-12-7517-2012, 2012.
- 759 Schervish, M. and Shiraiwa, M.: Impact of phase state and non-ideal mixing on equilibration
760 timescales of secondary organic aerosol partitioning, *Atmos. Chem. Phys.*, 23, 221-233,
761 10.5194/acp-23-221-2023, 2023.

- 762 Seinfeld, J. H. and Pandis, S. N.: Atmospheric chemistry and physics: from air pollution to
763 climate change, John Wiley & Sons 2016.
- 764 Shiraiwa, M. and Pöschl, U.: Mass accommodation and gas–particle partitioning in secondary
765 organic aerosols: dependence on diffusivity, volatility, particle-phase reactions, and penetration
766 depth, *Atmos. Chem. Phys.*, 21, 1565-1580, 10.5194/acp-21-1565-2021, 2021.
- 767 Shiraiwa, M., Ammann, M., Koop, T., and Pöschl, U.: Gas uptake and chemical aging of
768 semisolid organic aerosol particles, *Proc. Nat. Acad. Sci.*, 108, 11003-11008,
769 10.1073/pnas.1103045108, 2011.
- 770 Shiraiwa, M., Berkemeier, T., Schilling-Fahnestock, K. A., Seinfeld, J. H., and Pöschl, U.:
771 Molecular corridors and kinetic regimes in the multiphase chemical evolution of secondary
772 organic aerosol, *Atmos. Chem. Phys.*, 14, 8323-8341, 10.5194/acp-14-8323-2014, 2014.
- 773 Shiraiwa, M., Yee, L. D., Schilling, K. A., Loza, C. L., Craven, J. S., Zuend, A., Ziemann, P.
774 J., and Seinfeld, J. H.: Size distribution dynamics reveal particle-phase chemistry in organic
775 aerosol formation, *Proceedings of the National Academy of Sciences of the United States of*
776 *America*, 110, 11746-11750, 10.1073/pnas.1307501110, 2013.
- 777 Shiraiwa, M., Li, Y., Tsimpidi, A. P., Karydis, V. A., Berkemeier, T., Pandis, S. N., Lelieveld,
778 J., Koop, T., and Pöschl, U.: Global distribution of particle phase state in atmospheric secondary
779 organic aerosols, *Nature Communications*, 8, 15002, 10.1038/ncomms15002, 2017.
- 780 Shrivastava, M., Lou, S., Zelenyuk, A., Easter, R. C., Corley, R. A., Thrall, B. D., Rasch, P. J.,
781 Fast, J. D., Massey Simonich, S. L., Shen, H., and Tao, S.: Global long-range transport and lung
782 cancer risk from polycyclic aromatic hydrocarbons shielded by coatings of organic aerosol,
783 *Proc. Nat. Acad. Sci.*, 114, 1246-1251, 2017.
- 784 Smith, N. R., Crescenzo, G. V., Huang, Y., Hettiyadura, A. P. S., Siemens, K., Li, Y., Faiola,
785 C. L., Laskin, A., Shiraiwa, M., Bertram, A. K., and Nizkorodov, S. A.: Viscosity and liquid–
786 liquid phase separation in healthy and stressed plant SOA, *Environmental Science:*
787 *Atmospheres*, 1, 140-153, 10.1039/D0EA00020E, 2021.
- 788 Song, M., Maclean, A. M., Huang, Y., Smith, N. R., Blair, S. L., Laskin, J., Laskin, A.,
789 DeRieux, W. S. W., Li, Y., Shiraiwa, M., Nizkorodov, S. A., and Bertram, A. K.: Liquid–liquid
790 phase separation and viscosity within secondary organic aerosol generated from diesel fuel
791 vapors, *Atmos. Chem. Phys.*, 19, 12515-12529, 10.5194/acp-19-12515-2019, 2019.
- 792 Srivastava, D., Vu, T. V., Tong, S., Shi, Z., and Harrison, R. M.: Formation of secondary
793 organic aerosols from anthropogenic precursors in laboratory studies, *npj Climate and*
794 *Atmospheric Science*, 5, 22, 10.1038/s41612-022-00238-6, 2022.
- 795 Tobias, H. J., Kooiman, P. M., Docherty, K. S., and Ziemann, P. J.: Real-Time Chemical
796 Analysis of Organic Aerosols Using a Thermal Desorption Particle Beam Mass Spectrometer,
797 *Aerosol Sci. Technol.*, 33, 170-190, 10.1080/027868200410912, 2000.
- 798 Valorso, R., Aumont, B., Camredon, M., Raventos-Duran, T., Mouchel-Vallon, C., Ng, N. L.,
799 Seinfeld, J. H., Lee-Taylor, J., and Madronich, S.: Explicit modelling of SOA formation from
800 α -pinene photooxidation: sensitivity to vapour pressure estimation, *Atmospheric Chemistry and*
801 *Physics*, 11, 6895-6910, 10.5194/acp-11-6895-2011, 2011.

802 Vereecken, L. and Peeters, J.: Decomposition of substituted alkoxy radicals—part I: a
803 generalized structure–activity relationship for reaction barrier heights, *Physical Chemistry*
804 *Chemical Physics*, 11, 9062-9074, 2009.

805 Verwer, J. G.: Gauss–Seidel iteration for stiff ODEs from chemical kinetics, *SIAM Journal on*
806 *Scientific Computing*, 15, 1243-1250, 1994.

807 Verwer, J. G., Blom, J. G., and Hundsdorfer, W.: An implicit-explicit approach for atmospheric
808 transport-chemistry problems, *Applied Numerical Mathematics*, 20, 191-209, 1996.

809 Virtanen, A., Joutsensaari, J., Koop, T., Kannosto, J., YliPirilä, P., Leskinen, J., Mäkelä, J. M.,
810 Holopainen, J. K., Pöschl, U., Kulmala, M., Worsnop, D. R., and Laaksonen, A.: An amorphous
811 solid state of biogenic secondary organic aerosol particles, *Nature*, 467, 824-827,
812 doi:10.1038/nature09455, 2010.

813 Ye, Q., Robinson, E. S., Ding, X., Ye, P., Sullivan, R. C., and Donahue, N. M.: Mixing of
814 secondary organic aerosols versus relative humidity, *Proc. Nat. Acad. Sci.*, 113, 12649-12654,
815 2016.

816 Zaveri, R. A., Wang, J., Fan, J., Zhang, Y., Shilling John, E., Zelenyuk, A., Mei, F., Newsom,
817 R., Pekour, M., Tomlinson, J., Comstock Jennifer, M., Shrivastava, M., Fortner, E., Machado
818 Luiz, A. T., Artaxo, P., and Martin Scot, T.: Rapid growth of anthropogenic organic
819 nanoparticles greatly alters cloud life cycle in the Amazon rainforest, *Science Advances*, 8,
820 eabj0329, 10.1126/sciadv.abj0329, 2022.

821 Zhang, X., Cappa, C. D., Jathar, S. H., McVay, R. C., Ensberg, J. J., Kleeman, M. J., and
822 Seinfeld, J. H.: Influence of vapor wall loss in laboratory chambers on yields of secondary
823 organic aerosol, *Proc. Nat. Acad. Sci.*, 111, 5802-5807, 2014.

824 Zhang, Y., Chen, Y., Lambe, A. T., Olson, N. E., Lei, Z., Craig, R. L., Zhang, Z., Gold, A.,
825 Onasch, T. B., Jayne, J. T., Worsnop, D. R., Gaston, C. J., Thornton, J. A., Vizuete, W., Ault,
826 A. P., and Surratt, J. D.: Effect of the Aerosol-Phase State on Secondary Organic Aerosol
827 Formation from the Reactive Uptake of Isoprene-Derived Epoxydiols (IEPOX), *Environmental*
828 *Science & Technology Letters*, 5, 167-174, 10.1021/acs.estlett.8b00044, 2018.

829 Zhang, Y., Nichman, L., Spencer, P., Jung, J. I., Lee, A., Heffernan, B. K., Gold, A., Zhang, Z.,
830 Chen, Y., Canagaratna, M. R., Jayne, J. T., Worsnop, D. R., Onasch, T. B., Surratt, J. D.,
831 Chandler, D., Davidovits, P., and Kolb, C. E.: The Cooling Rate- and Volatility-Dependent
832 Glass-Forming Properties of Organic Aerosols Measured by Broadband Dielectric
833 Spectroscopy, *Environ. Sci. Technol.*, 53, 12366-12378, 10.1021/acs.est.9b03317, 2019.

834 Zhao, B., Wang, S., Donahue, N. M., Jathar, S. H., Huang, X., Wu, W., Hao, J., and Robinson,
835 A. L.: Quantifying the effect of organic aerosol aging and intermediate-volatility emissions on
836 regional-scale aerosol pollution in China, *Sci. Rep.*, 6, 28815, 10.1038/srep28815, 2016.

837 Zhou, S., Hwang, B. C. H., Lakey, P. S. J., Zuend, A., Abbatt, J. P. D., and Shiraiwa, M.:
838 Multiphase reactivity of polycyclic aromatic hydrocarbons is driven by phase separation and
839 diffusion limitations, *Proc. Nat. Acad. Sci.*, 116, 11658-11663, 10.1073/pnas.1902517116,
840 2019.

841 Ziemann, P. J. and Atkinson, R.: Kinetics, products, and mechanisms of secondary organic
842 aerosol formation, *Chemical Society Reviews*, 41, 6582-6605, 2012.

843 Zobrist, B., Marcolli, C., Pedernera, D. A., and Koop, T.: Do atmospheric aerosols form
844 glasses?, *Atmospheric Chemistry and Physics*, 8, 5221-5244, 2008.
845
846

847 **Appendix.**

848

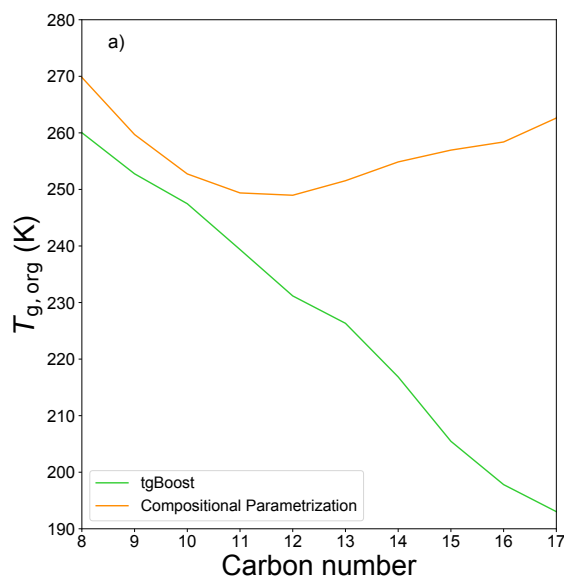
849 **Table A1:** Experimental and simulated functional group distributions, O:C and N:C ratios of
 850 SOA generated from C16 oxidation by OH in presence of high NO_x.

FG/C16 molecule	Experimental	Simulated (tgBoost)	Simulated (CP)
Nitrate	0.91	0.65	0.54
Carbonyl	0.38	0.26	0.15
Hydroxyl	0.41	0.43	0.45
Carboxyl	0.09	0.0	0.0
Ester	0.28	0.2	0.07
Peroxide	0.12	0.01	0.0
Methylene	13.81	12.12	12.07
O:C	0.28	0.25	0.25
N:C	0.06	0.04	0.03
H:C	1.85	/	/
MW	294	/	/
Density (g cm ⁻³)	1.10	1.06	1.06

851

852

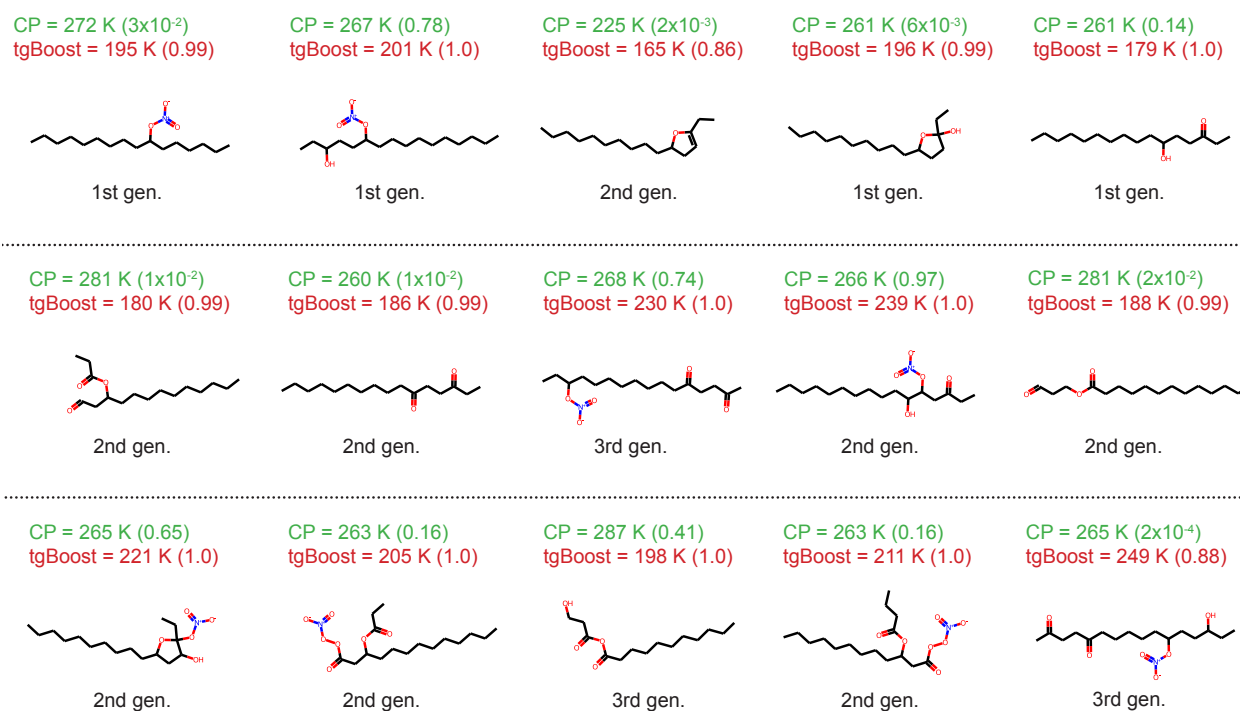
853



854

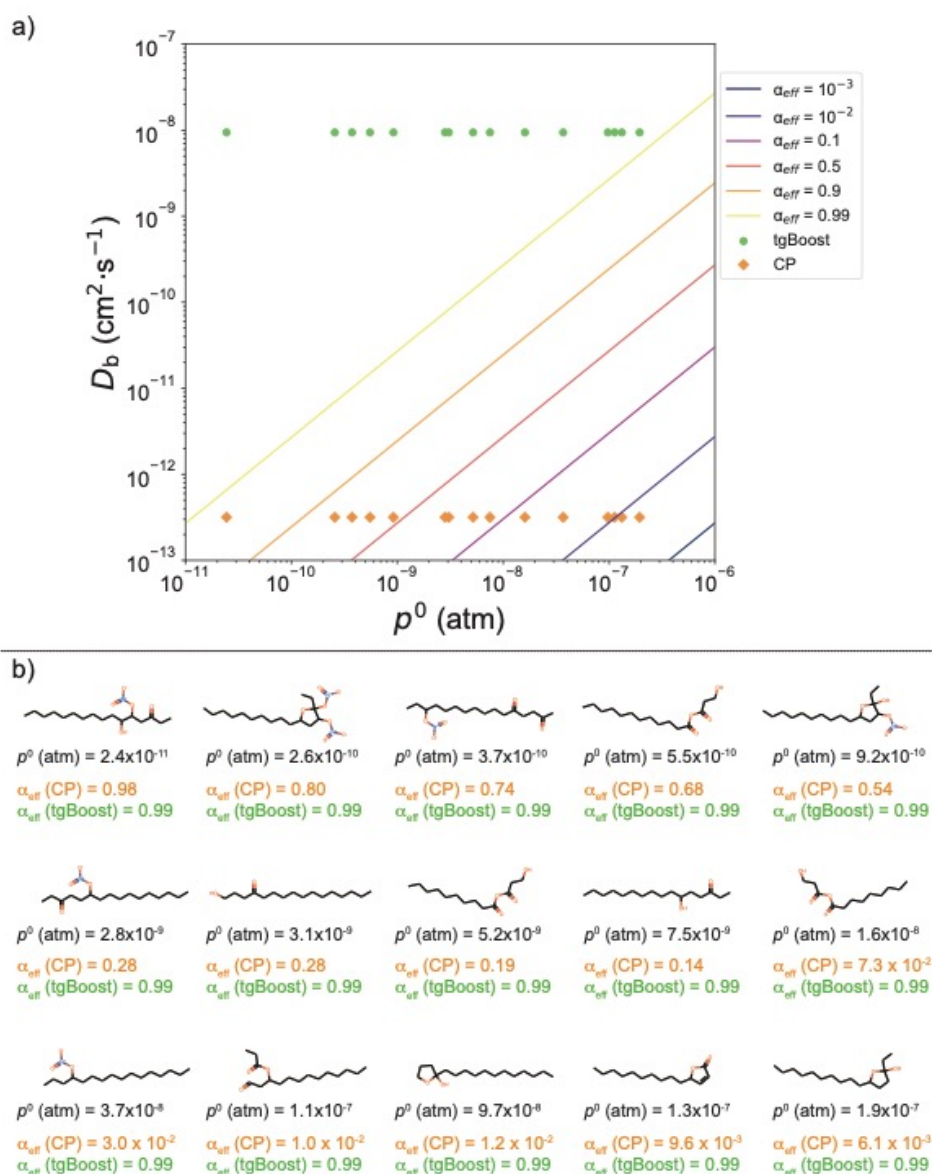
855 **Figure A1:** Predicted $T_{g,org}$ of SOA generated from n-alkanes as computed by the GECKO-A
 856 box model with the T_g compositional parametrization (orange line) and tgBoost (green line) at
 857 the last step of the simulations ($t = 3600$ s).

858



859
860
861
862
863
864
865
866
867

Figure A2. Top 15 species with highest concentrations in oxidation products of n-hexadecane ($C_{16}H_{34}$) under high NO_x conditions simulated by GECKO-A with effective mass accommodation coefficient (α_{eff}) with the compositional parameterization. The species are reported in descending concentrations from left to right and from top to bottom. Listed values are T_g as calculated by tgBoost and CP and α_{eff} values at the end of simulation (3600 s) in brackets. Types of compounds are also noted (1st, 2nd, and 3rd generation products, decomposition products).



868

869 **Figure A3.** a) α_{eff} isolines as a function of bulk diffusivity D_b and saturation vapor pressure
 870 p^0 of semi-volatile species. b) Selection of various representative SOA contributors produced
 871 during the oxidation of n-hexadecane. The species are ordered by decreasing vapor pressure.
 872 The reported α_{eff} values for each SOA contributor are calculated for D_b estimated with tgBoost
 873 ($D_b = 1 \times 10^{-8} \text{ cm}^2 \text{ s}^{-1}$) and CP ($D_b = 3 \times 10^{-13} \text{ cm}^2 \text{ s}^{-1}$). The values of α_{eff} for the selected species
 874 are reported as points in the top panel. It shows that for the liquid-like state estimated with the
 875 tgBoost configuration, α_{eff} tend towards 1 for all species. This behavior is not observed in the
 876 amorphous semi-solid state estimated using the CP model configuration for species with p^0
 877 above 10^{-9} atm. For the simulated conditions, species with p^0 between 10^{-8} and 10^{-6} atm are of
 878 enough low volatility to partition between the particle and gas phases at equilibrium. For species
 879 in that volatility range, no mass transfer limitation is observed with the tgBoost configuration,
 880 unlike the CP configuration. Using the CP configuration, the most volatile SOA contributors
 881 are subjected to substantial mass transfer limitation and are therefore mainly eliminated by gas-
 882 phase oxidation or wall deposition.
 883